Effect of heating temperature on structural, magnetic, and dielectric properties of Magnesium ferrites prepared in the presence of *Solanum Lycopersicum* fruit extract

Hina N. Chaudhari[1], Preksha N. Dhruv[1], Charanjeet Singh[2,*], Sher Singh Meena[3,*], Shrikanti Kavita[4], and Rajshree B. Jotania[1,*] [iD]

[1] Department of Physics, Electronics and Space Science, University School of Sciences, Gujarat University, Ahmedabad 380 009, India

[2] School of Electronics and Electrical Engineering, Lovely Professional University, Jalandhar, Punjab 144 411, India

[3] Solid State Physics Division, Bhabha Atomic Research Centre, Mumbai 400085, India

[4] International Advanced Research Centre for Powder Metallurgy and New Materials (ARCI), IIT Chennai Research Park, Chennai 600113, India

ABSTRACT

$MgFe_2O_4$ ferrite was synthesized in the presence of *Solanum Lycopersicum* fruit extract using sol–gel auto-combustion technique and heated from 650 °C to 1050 °C with the difference of 100 °C. The effect of heating temperature on phase purity, crystal structure, and magnetic as well as dielectric properties was systematically investigated. XRD analysis show that all samples consist of a single phase cubic spinel structure. The average crystallite size of heated samples varied from 10 to 26 nm, it was observed that crystallite size increases with the calcination temperature and average grain size was found in between 18 and 65 nm. SEM micrographs show that there is a drastic reduction in the grain size in the sample prepared in presence of tomato extract (65 nm) compared to the sample prepared without tomato extract (373 nm) and heated at 1050 °C for 4 h. All samples belong to soft ferrite ($H_C \sim$ 10 to 70 Oe) and possess a multi-domain structure. As heating temperature increases the values of both saturation magnetization (M_S) and hyperfine magnetic field (H_{hf}) are found to increase. The frequency-dependent dielectric phenomenon was observed in all prepared samples and single one-fourth semi-circles observed in Nyquist plot because of the contribution of the grain boundaries over the grain conductions. M'' and Z'' vs frequency plots reveal the absence of Debye relaxation in prepared compositions.

1 Introduction

Ferrites are ferrimagnetic ceramics that comprise iron oxide as the main element [1]. Ferrites have huge technological importance due to their good magnetic and electrical properties [2, 3]. Spinel ferrites are used in various gadgets like high-frequency transformer cores, phase shifter, switches, resonators, mobile phones, computers, and televisions [4, 5]. Nanoparticles of spinel ferrites are used for gas sensor and hyperthermia applications [6–8]. Ferrites with spinel structure can be represented by MFe_2O_4 (where, $M = Ni^{2+}$, Co^{2+}, Cu^{2+}, etc.). The cubic spinel ferrite has two sites: A (tetrahedral) and B (octahedral). According to site preference of cations, they are divided into three groups: normal spinel, inverse spinel, and mixed spinel. If a tetrahedral site is occupied by divalent metal ions, and an octahedral site occupied by trivalent ions, then it is called normal spinel ferrite, whereas if an octahedral site is occupied by divalent metal ions, and a tetrahedral site is occupied by trivalent ions then it is known as inverse spinel ferrite. If the divalent cations are present on both tetrahedral and octahedral sites, the spinel is called as mixed spinel ferrite. $ZnFe_2O_4$, $NiFe_2O_4$, and $MnFe_2O_4$ are normal spinel, inverse spinel, and mixed spinel ferrites, respectively [9]. Spinel ferrites can be prepared using various synthesis techniques like standard ceramic [10, 11], microwave hydrothermal [12], coprecipitation [13], ball milling [14], microemulsion [15], and sol–gel auto-combustion [16, 17] method. In the present study, we have adopted the sol–gel auto-combustion method to prepare $MgFe_2O_4$ ferrite powder because the sol–gel method is suitable to attain homogeneous ions at an atomic level in the precursor [18]. The advantage of this method is low processing cost due to the short exothermic reaction time and a homogeneous powder is obtained.

The magnetic properties of the MgCd ferrite system were reported by Upadhyay et al. [19], whereas magnetic and electrical properties of Al^{3+}-substituted $MgFe_2O_4$ were investigated by K.B. Midi et al. [20]. Faezeh Gandomi and his co-workers [21] reported photocatalytic and anticancer activities of magnesium-doped lithium nanoferrites ($Li_{0.5}Fe_{2.5}O_4$) prepared using the sol–gel method. Recently, the influence of Yb^{3+} and Pr^{3+} substitution in cobalt–nickel ferrite on the magnetic properties, cytotoxic, and photocatalytic activities was evaluated by Seyed Mahdi Peymani-

Motlag et al. It was observed that Yb^{3+}-substituted cobalt–nickel ferrite (with lower M_r, M_s, H_c) shows higher efficiency compared to Pr^{3+}-substituted cobalt–nickel ferrite under UV light [22]. $CuFe_{2-x}Ce_xO_4$ nanoparticles (crystallite size 52 nm) were successfully synthesized by the auto-combustion sol–gel method and the effect of different capping agents (lactose and glucose), with different concentrations on the morphology and particle size was investigated by Mehdi Rahimi–Nasrabadi et al. [23].

Currently, many researchers are working on green chemistry to improve and protect our environment. The development of biodegradable and cost-efficient synthesis methods of nanoparticle still remains a scientific challenge. Nanotechnology is playing an important role in eliminating environmental issues caused by chemical industries such as oils, organic dyes, mercury, and waste water. The nanoparticles synthesized by chemical methods involve harmful chemicals that may affect the human body and environment. Hence, biological approaches using plants or plant extracts for synthesis of nanoparticles are important alternatives to chemicals. Manikandan et al. [24] have prepared $CuFe_2O_4$ spinel ferrites in the presence of Hibiscus Rosa-Sinensis leaf extract, using both modified microwave heating technique and sol–gel technique. The coercivity was found 351.57 Oe and 173.59 Oe with the saturation magnetization of 61.13 emu/g and 57.25 emu/g, respectively. D. Gingasu et al. [25] have synthesized polycrystalline $CoFe_2O_4$ spinel ferrites using the aqueous extract of ginger root and cardamom seed and obtained a pure spinel phase structure with good crystallinity. Ben–Arfa et al. [26] have synthesized magnetic spinel ferrite in the presence of clove and cinnamon extracts from only iron nitrate. Fardood et al. [27] have prepared Ni–Cu–Mg ferrite nanoparticles using tragacanth gum and reported an average particle size of 19 nm. Kombaiah et al. [28] have synthesized $CoFe_2O_4$ nanoparticles using okra extract.

There has been a huge attention in using natural plant or plant extracts as fuels. Some of them combine sustainability and anti-oxidative properties [26]. Tomato contains vitamin C (23 mg/100 g) compared to other vegetables such as carrot (2 mg/100 g), potatoes (14 mg/100 g), and spinach (10 mg/100 g) [29] that plays an essential role in a chelating process for the formation of ferrite. Tomato (*Solanum Lycopersicum*) is a fruit of a perennial plant in the *Solanaceae*
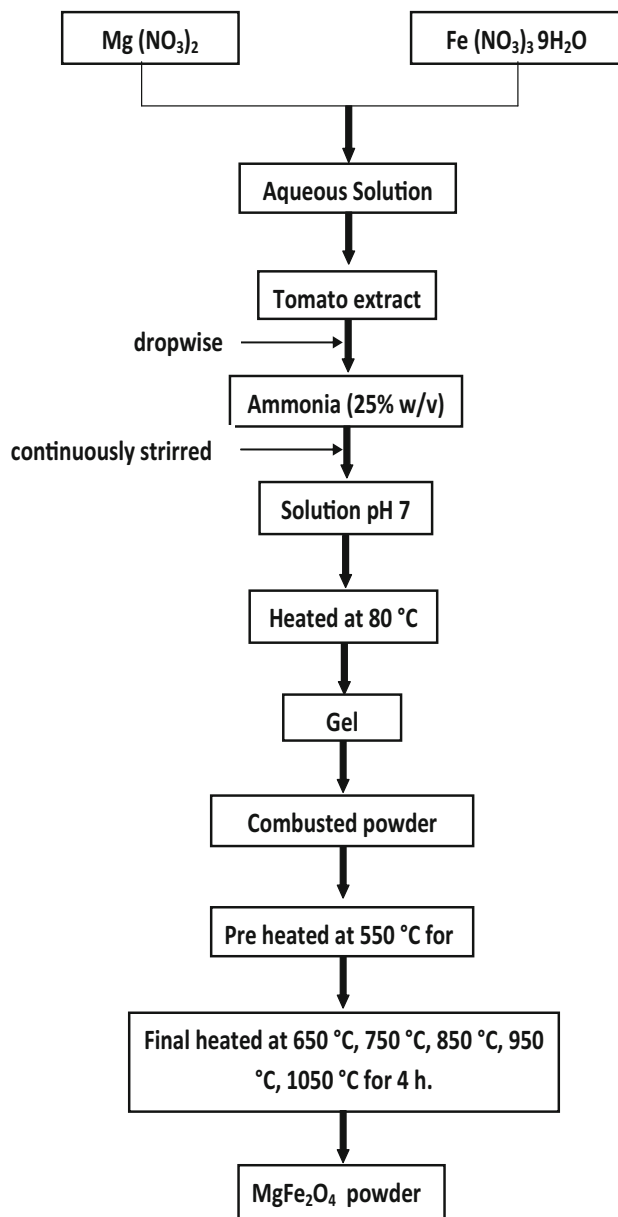
Fig. 1 Flowchart for the preparation of MgFe$_2$O$_4$ ferrite powder

family [30]; it's also contains *lycopene* that helps in preventing cancer and diabetes [31].

Tomatoes are easily available in market throughout the year and contain vitamin C (23 mg/100 g); so tomato can be used as a fuel in sol–gel process instead of citric acid. In present synthesis, tomato is also used as green reducing agent for the preparation of magnesium ferrite.

Magnesium ferrite (MgFe$_2$O$_4$) has been found excellent applications in color imaging, high-frequency devices, sensors, high-density magnetic recording, electronic devices, microwave absorbents,

and magnetic materials [32–35]. MgFe$_2$O$_4$ is a normal spinel, but magnetically soft [36, 37] ferrite. The physical and chemical properties of MgFe$_2$O$_4$ depend upon the cations distribution among A and B sites of crystal lattice [38]. The aim of the present work is to investigate the effect of heating temperature on structural, magnetic, surface morphology, and dielectric properties of MgFe$_2$O$_4$ ferrite powder prepared in the presence of tomato fruit extract. To the best of our knowledge, no research has been conducted so far to study the synthesis and characterization of MgFe$_2$O$_4$ ferrite using tomato fruit extract as green reducing agent.

2 Experimental method

2.1 Materials

Magnesium nitrate Mg(NO$_3$)$_2$·6H$_2$O (99% pure, Merck Specialities, Mumbai, India), Ferric nitrate (Fe(NO$_3$)$_3$·9H$_2$O, 99% pure, HPLC, Mumbai, India), Ammonia solution (25% w/v, Merck specialities Pvt. Ltd, Mumbai, India), and Tomatoes.

2.2 Preparation of tomato fruit extract

Tomatoes (∼ 500 g.) were bought from local vegetable market (Ahmedabad, Gujarat, India), washed with tap water and then by distilled water, and kept at room temperature for natural drying. Tomatoes were finely cut and then grinded in a mixture for 3 min. 100 ml of distilled water was added in to 100 ml of thick tomato mixture and stirred well for 15 min. The obtained mixture was kept on a hot plate at 80 °C under constant stirring for 5 min and then gradually cooled down at room temperature. The prepared tomato mixture was filtered to recover yellowish tomato extract.

2.3 Experimental procedure

First of all, magnesium nitrate and ferric nitrate were taken in stoichiometric amount and dissolved separately in 100 ml of distilled water, then mixed together, and kept on a magnetic stirrer for 15 min. 100 ml of tomato fruit extract was added drop wise into as prepared metal nitrate solution and heated at ∼ 42 °C on a hot plate under constant stirring. Thereafter, prepared solution was neutralized
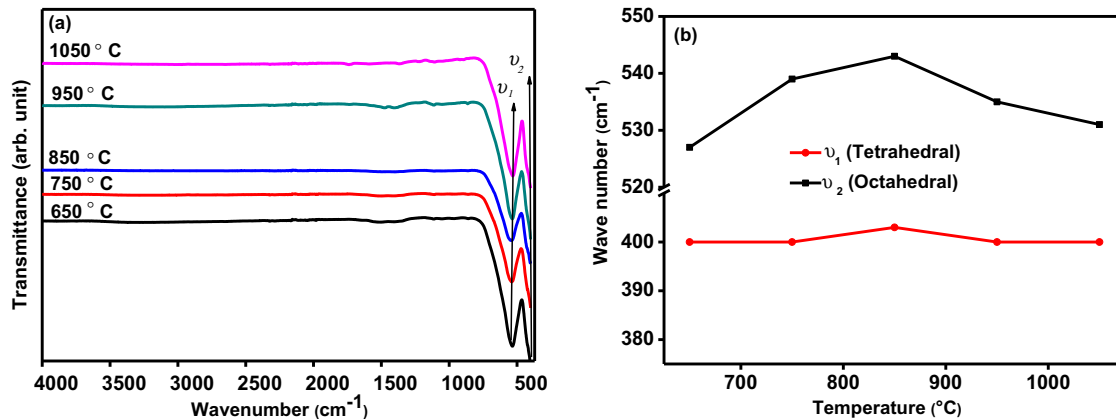
Fig. 2 **a** FTIR spectra of MgFe$_2$O$_4$ ferrite synthesized in the presence of *solanum lycopersicum* extract heated at 650 °C, 750 °C, 850 °C, 950 °C, and 1050 °C, **b** variation in tetrahedral (v_1) and octahedral (v_2) sites with heating temperature

(pH ∼ 7) by adding ∼ 20 ml of ammonia (25% w/v) solution. Further, as obtained dark greenish solution was kept on a hot plate at 80 °C until it transformed into a viscous brown gel; on further heating of gel, ignition initiated and a self-propagating combustion process started to form dark brown ash. The obtained ash was grinded finely and pre-heated at 550 °C for 4 h. in a muffle furnace. Finally pre-heated ash was sintered at 650 °C, 750 °C, 850 °C, 950 °C, and 1050 °C for 4 h and then slowly cooled to room temperature to obtain MgFe$_2$O$_4$ ferrite powder. The schematic representation for preparation of magnesium ferrite powder is shown in Fig. 1.

2.4 Characterizations

The FTIR spectrometer (Perkin Elmer Spectrum-two) was used to record FTIR spectra of heated samples in wavenumber range from 4000–400 cm^{-1}. X-ray diffractograms of all samples were scanned from 20°–80° using a X-ray diffractometer (Rotaflex RU-200). The Quanta 200 FEG scanning electron microscope (SEM) was used to examine the surface morphology of prepared samples. For the high-resolution microscopic analysis, FE-SEM was also used (Make: Zeiss, Model: Auriga). Magnetic hysteresis loops were recorded at room temperature on VSM (EZ9, Microsense Inc, USA) under an applied magnetic field of ± 20 kOe. A conventional spectrometer was used to record Mössbauer spectra (MS) at room temperature. A Mössbauer spectrometer was activated in transmission geometry (continuous acceleration mode) using Co^{57} source embedded in the Rh matrix of 50 mCi. The recorded Mössbauer spectra were

fitted using WinNormos site fit program. An α-^{57}Fe metal foil was used for the calibration of the velocity scale. The isomer shift values are associated with Fe metal foil where δ = 0.0 mm/s. The low-frequency dielectric measurements were carried out at room temperature using a LCR meter (Agilent E 4980A) in the frequency range from 10 kHz to 2 MHz.

3 Results and discussion

3.1 Structural properties

3.1.1 FTIR analysis

Figure 2a represents the FTIR spectra of MgFe$_2$O$_4$ ferrite powder samples heated at 650 °C, 750 °C, 850 °C, 950 °C, and 1050 °C for 4 h. It can be seen from Fig. 2a that all samples show two distinct absorption bands; the high-frequency band (v_1) lies in a wave number range of 650–530 cm^{-1} and the low-frequency band (v_2) lies in between 446–400 cm^{-1} due to intrinsic stretching vibrations of Fe–O among tetrahedral (A) and octahedral (B) sites, respectively, which signify that the spinel phase was formed [18]. The position of these bands is changing (as shown in Fig. 2b) which is attributed to the different bond length among tetrahedral and octahedral sites [39–41].

3.1.2 XRD analysis

The crystal structure and phase purity of the prepared samples were verified using XRD technique. Figure 3a illustrates the X-ray diffraction patterns of

Fig. 3 a XRD patterns of $MgFe_2O_4$ prepared in the presence of *solanum lycopersicum* extract heated at different temperatures. **b** Variation in lattice constant (*a*) and unit cell volume (V_{cell}) with increasing the heating temperature. **c, d** Rietveld-refined XRD patterns of $MgFe_2O_4$ samples heated at 650 °C and 1050 °C, respectively
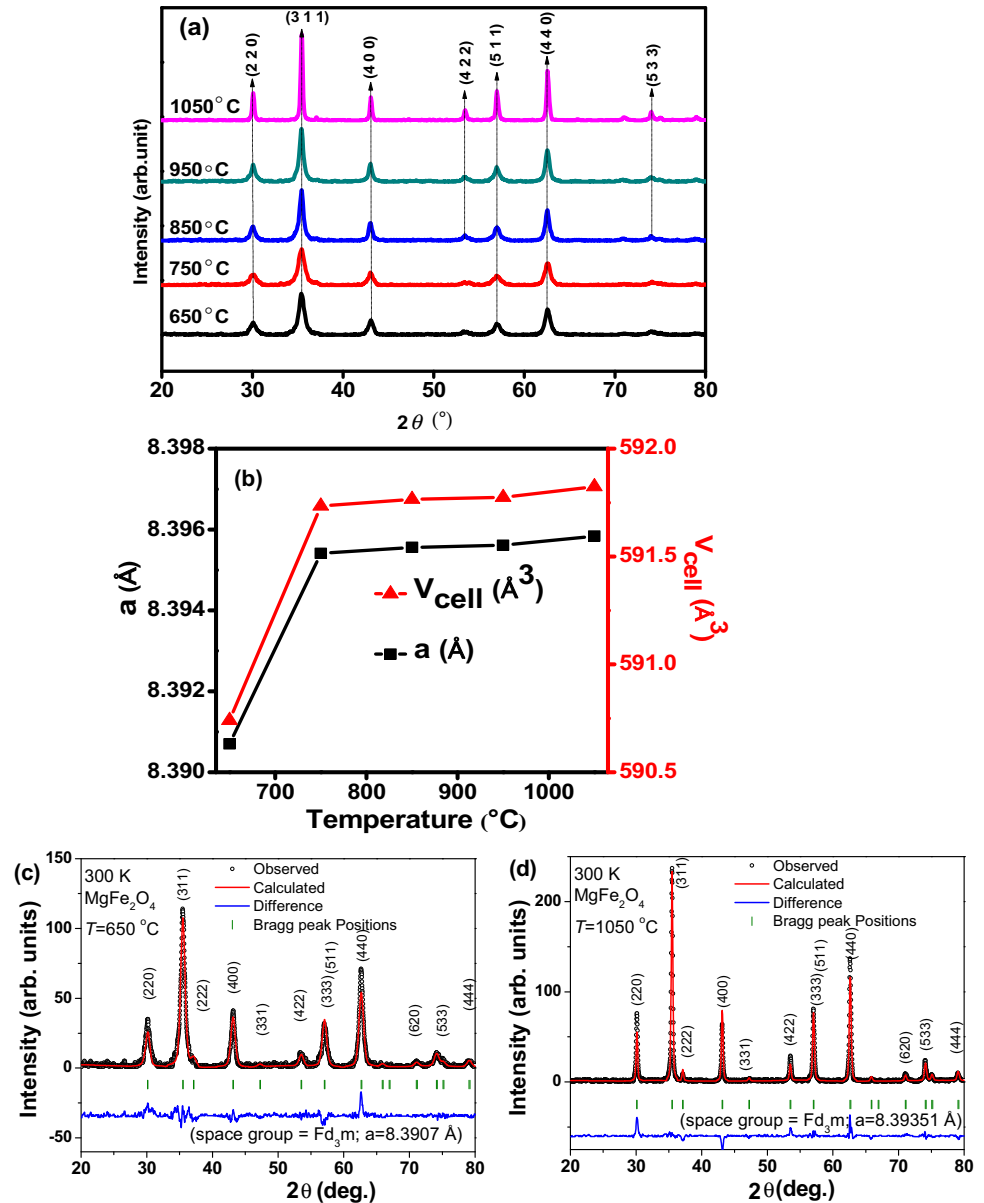

Table 1 Structural parameters of $MgFe_2O_4$ synthesized in the presence of *solanum lycopersicum* extract and heated at different temperatures for 4 h

Heating temperature (°C)	2θ (°)	d spacing (Å)	Lattice parameter a (Å)	Unit cell volume V_{cell} (Å)^3	Average crystallite size D_{xrd} (nm)	FWHM (°)
650	35.427	2.531	8.3907	590.741	9.57	0.829
750	35.400	2.533	8.39541	591.734	10.75	0.738
850	35.427	2.531	8.39556	591.765	15.00	0.532
950	35.408	2.533	8.39561	591.774	15.05	0.527
1050	35.438	2.530	8.39584	591.824	26.00	0.305

Table 2 The bulk density, X-ray density, and porosity of MgFe$_2$O$_4$ ferrites synthesized in the presence of *solanum lycopersicum* extract and heated at different temperatures for 4 h

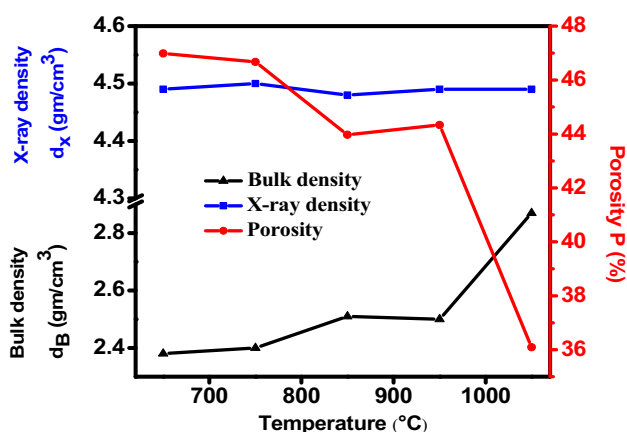| Heating temperature (°C)	Bulk density d_B (g/cm^3)	X-ray density d_x (g/cm^3)	Porosity P (%)
650	2.38	4.49	46.99
750	2.40	4.50	46.67
850	2.51	4.48	43.97
950	2.50	4.49	44.33
1050	2.87	4.49	36.09

Fig. 4 Variation in bulk density, X-ray density, and porosity of MgFe$_2$O$_4$ samples with increasing the heating temperature

Magnesium spinel ferrite samples synthesized in the presence of *Solanum Lycopersicum* extract and heated at 550 °C, 650 °C, 750 °C, 850 °C, 950 °C, and 1050 °C for 4 h. The variation of the unit cell volume and lattice parameter with heating temperature is represented in Fig. 3b–d which show the Rietveld-refined XRD patterns of MgFe$_2$O$_4$ sample heated at 650 °C and 1050 °C for 4 h. The Rietveld refinement has been done by using a FullProf program.

The major reflection planes correspond to (220), (311), (400), (422), (511), (440), (620), (533), and (444) in all samples that match well with JCPDS file PDF # 88-1943. It can be seen from Fig. 3a that (311) peak displays the strongest reflection compared to other Bragg peaks, which indicates that formed ferrite samples possess a single phase with space group Fd_3m [42]. The values of d-spacing, FWHM, lattice parameter, and crystallite size of all samples are listed in Table 1. It can be observed from Fig. 3a that as heating temperature of the samples increases the diffraction peak (311)

Fig. 5 SEM images of MgFe$_2$O$_4$ ferrites synthesized in the presence of *solanum lycopersicum* extract, heated at 650 °C (**a**), 750 °C (**b**), 850 °C (**c**), 950 °C (**d**), 1050 °C (**e**), and 1050 °C (**g**) for 4 h. (**h**) SEM image of MgFe$_2$O$_4$ ferrites synthesized without *solanum lycopersicum* extract, heated at 1050 °C for 4 h. **f** EDX spectra of MgFe$_2$O$_4$ ferrites synthesized in the presence of *solanum lycopersicum* extract and heated at 650 °C for 4 h. **i**, **j** Histograms of grain size for MgFe$_2$O$_4$ ferrites synthesized with (SEM image g) and without (SEM image h) *solanum lycopersicum* extract, respectively, heated at 1050 °C for 4 h

becomes sharper, which reflects higher crystallization of prepared samples. The variation in lattice parameters (8.3907 Å-8.3958 Å) at different heating temperature implies that there is a variation in the cations distribution between both A and B sites, which is confirmed by Mössbauer spectroscopy [described in Sect. 3.4.2]. The value of the lattice parameter was reported by Sabah M. Ali Ridha et al. and is closer to our results [43]. The unit cell volume decreases as the lattice parameter decreases because unit cell volume is proportional to the lattice parameter. The crystallite size of all samples are determined using the Debye–Scherrer formula and is found to be increased (Table 1) with the heating temperature and they are lying in the range between 10 and 26 nm. These results achieve that the heating temperatures employ the grain growth of the ferrite phase. The crystallite size less than 50 nm is fascinating for obtaining a suitable signal-to-noise ratio for switching application [44]. As the temperature increases, the values of FWHM decrease. This observation shows that the heating temperature has the significant role in the formation of pure spinel ferrites.

3.1.3 Physical properties

The values of X-ray density, bulk density, and porosity of heated samples are presented in Table 2. Figure 4 depicts the variation in bulk density (d_B), X-ray density (d_x), and porosity (P) of MgFe$_2$O$_4$ spinel ferrites synthesized in the presence of *Solanum Lycopersicum* extract heated at various temperatures. It is clearly observed from Table 2 that an increase in temperature caused an increase in bulk density (d_B), and as a result, the porosity decreases through diffusion kinetics [43]. X-ray density is inversely proportional to the lattice constant. So as the temperature increases, lattice constant decreases slightly which results in an expected increase in the X-ray density. The porosity shows a decreasing trend (Table 2).
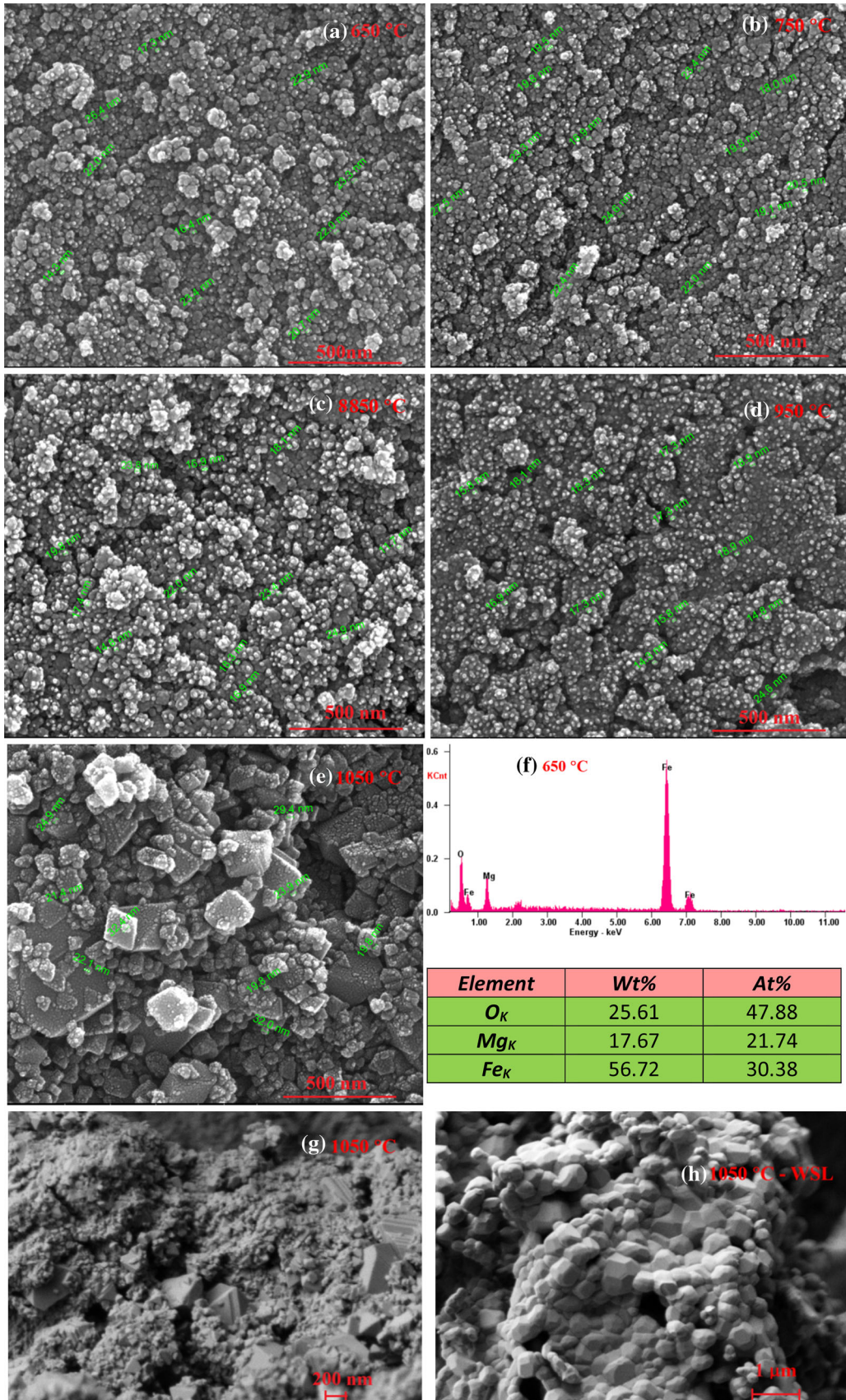
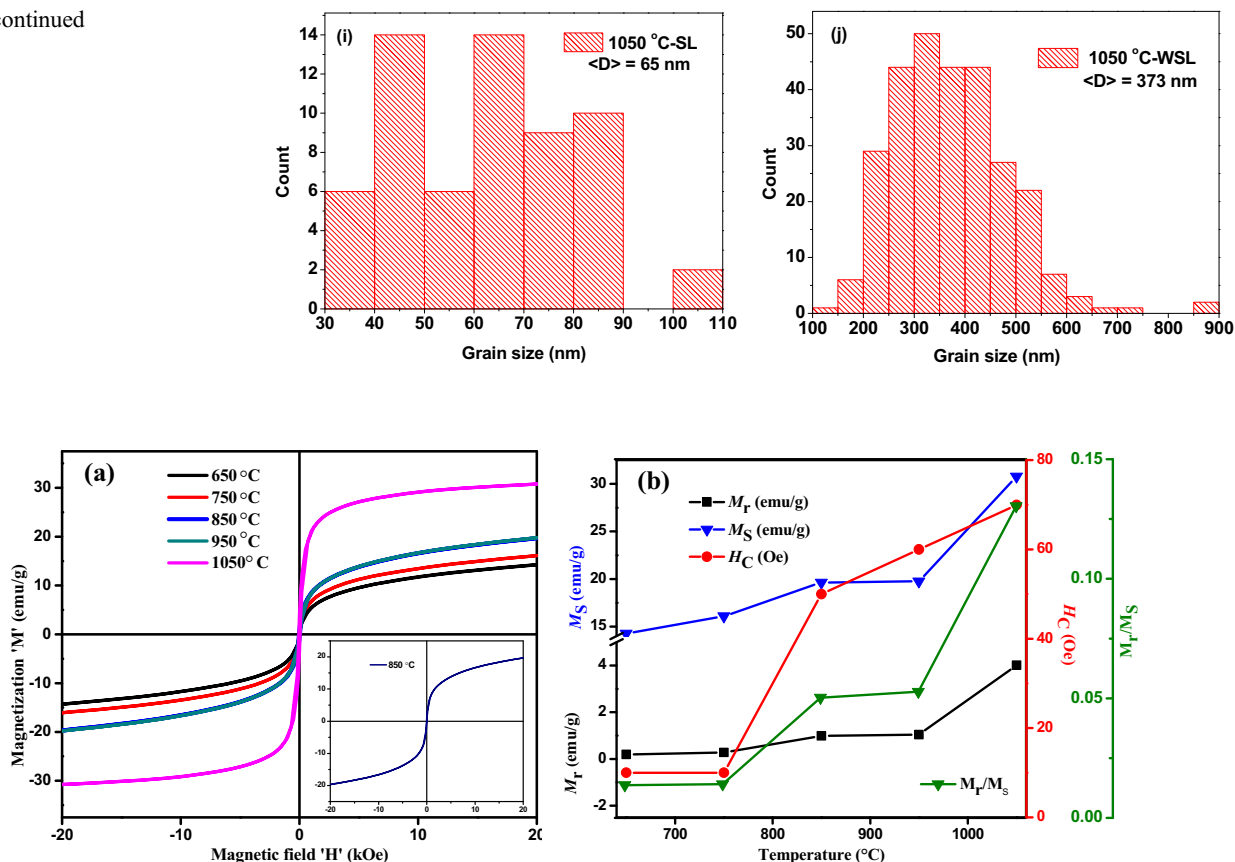| Element	Wt%	At%
O_K	25.61	47.88
Mg_K	17.67	21.74
Fe_K	56.72	30.38

Fig. 5 continued

Fig. 6 **a** M–H loops of MgFe$_2$O$_4$ synthesized in the presence of *solanum lycopersicum* extract heated at various temperature. **b** Variation in remanence magnetization (M_r), saturation magnetization (M_S), coercive field (H_C), and squareness ratio (M_r/M_S) with temperature

3.2 Surface morphology

The SEM micrograph gives information about the surface morphology and microstructure of synthesized material. SEM images of MgFe$_2$O$_4$ samples heated at 650 °C, 750 °C, 850 °C, 950 °C, and 1050 °C are shown in Fig. 5a–e. It is clear from Fig. 5a–d that formed grains are agglomerated and stick together by magnetic interactions, due to the intense forces of Vander Waals attraction [45]. It is interesting to note that the sample heated at 1050 °C (Fig. 5e) shows bigger grains compared to other samples. The samples of Fig. 5g and h are heated at same temperature (1050 °C), but the only difference is with (Fig. 5g and without Fig. 5h) tomato extract. Figure 5i, j presented the histograms of grain size for MgFe$_2$O$_4$ ferrites synthesized with (SEM image g) and without (SEM image h) *solanum lycopersicum* extract, respectively, heated at 1050 °C for 4 h. It is clear from Fig. 5g, h

that there is a drastic reduction in the grain size in the sample prepared in presence of tomato extract (65 nm) compared to the sample prepared without tomato extract (373 nm) and heated at 1050 °C for 4 h.

3.3 Energy dispersive X-ray (EDX) analysis

The EDX analysis precisely provides an estimation of the elemental attentiveness as per specifications of mixed chemicals at the time of preparation. The EDX spectra of the magnesium spinel ferrites (MgFe$_2$O$_4$) sample heated at 650 °C for 4 h. is represented in Fig. 5f. The existence of Fe, Mg, and O elements in MgFe$_2$O$_4$ spinel ferrite powder can be seen in the EDX spectra of the sample heated at 650 °C for 4 h.

Table 3 Magnetic parameters of $MgFe_2O_4$ synthesized in the presence of *solanum lycopersicum* fruit extract and heated at different temperatures for 4 h

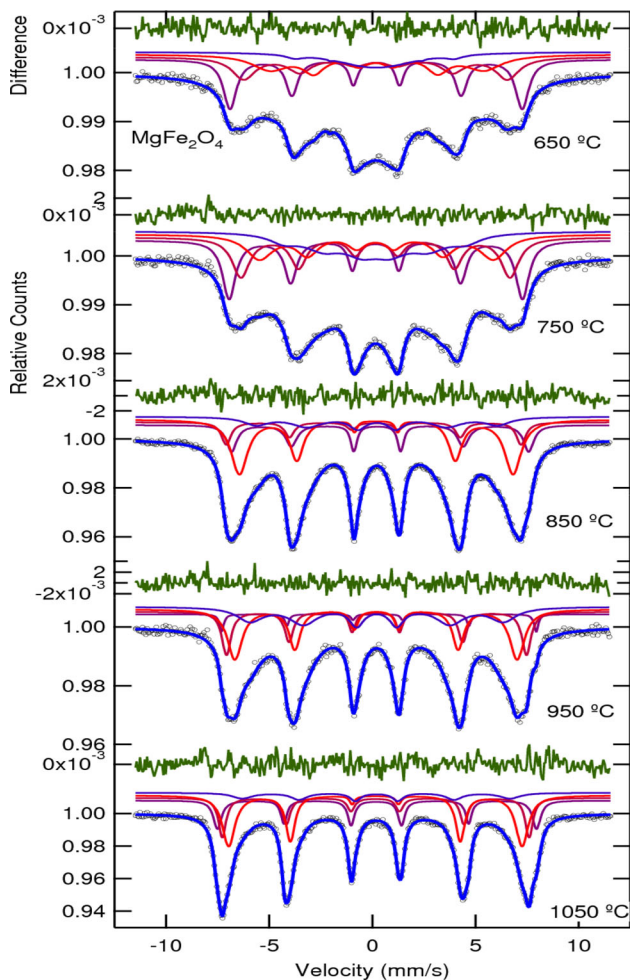| Heating temperature (°C)	Saturation Magnetization M_S (emu/g)	Remanence Magnetization M_r (emu/g)	Squareness ratio M_r/M_S	Coercivity H_C (Oe)	Ha (kOe)
650	14.28	0.196	0.0137	7.8	23.044
750	16.09	0.227	0.0141	9.4	23.890
850	19.63	0.988	0.0503	43	22.212
950	19.75	1.044	0.0528	52	22.389
1050	30.80	4.017	0.1304	62	13.435

Fig. 7 Room temperature Mössabauer spectra of $MgFe_2O_4$ spinel ferrites synthesized in the presence of *solanum lycopersicum* fruit extract heated at various temperature

4 Magnetic properties

4.1 Magnetic hysteresis loops analysis

Figure 6a represents magnetic hysteresis loops recorded at room temperature under an applied magnetic field of ± 20 kOe. The magnetic parameters obtained from hysteresis loops are listed in Table 3. In prepared samples, M_S is observed to increase from 14.28 emu/g. to 30.80 emu/g and H_C also increased from 7.8 Oe to 62 Oe. M_r value is found to increase from 0.19 emu/g to 4.01 emu/g with increasing heating temperature of samples.

The variation in saturation magnetization (M_S), remanence magnetization (M_r), coercivity (H_C), and squareness ratio (M_r/M_S) with temperature are presented in Fig. 6b. It shows that as the temperature increases, the value of M_r and M_S increases except the sample heated at 750 °C, while the sample heated at 1050 °C shows maximum value compared to other samples. It can be seen from Fig. 6b that M_S decreases a little when the temperature increases from 650 °C to 750 °C; thereafter, it increases significantly at 850 °C, 950 °C, and 1050 °C. The saturation magnetization in the spinel structure is due to the combination of lattice parameters and the arrangement of cations between tetrahedral and octahedral sites [46]. The mechanism of variation in M_S has been discussed in Mössbauer section. All samples show a characteristic of soft magnetic material [47]. The squareness ratio < 0.5 signifies that the materials have multi-domain structure while more than 0.5 indicates that the materials have a single-domain structure. In recent investigation, squareness ratio is found between 0.01 and 0.1 indicating that prepared samples possess a multi-domain structure [48].

Table 4 Results of Mössbauer spectral analysis at room temperature for MgFe$_2$O$_4$ ferrite samples synthesized in the presence of *solanum lycopersicum* fruit extract and heated at different temperatures for 4 h

Heating temperature (°C)	Iron Sites (Fe^{+3})	Hyperfine field (H_{hf}) Tesla ± 0.2	Isomer shift(δ) mm/s ± 0.02	Quadrupole splitting (Δ) mm/s ± 0.03	Line width (Γ) mm/s ± 0.1	Area R_A (%)
650	Sextet 1-oct	43.92	0.30	− 0.01	0.51	11.3
	Sextet 2-tet	39.64	0.28	− 0.03	1.36	24.3
	Sextet 3-oct	32.15	0.30	0.06	1.12	21.2
	Sextet 4-oct	23.94	0.25	− 0.07	3.89	43.2
750	Sextet 1-oct	44.10	0.27	0.008	0.51	12.5
	Sextet 2-tet	40.45	0.28	− 0.05	0.81	18.4
	Sextet 3-oct	35.17	0.28	0.05	1.02	21.4
	Sextet 4-oct	27.28	0.26	− 0.04	2.10	47.7
850	Sextet 1-oct	44.65	0.42	0.14	0.36	15.7
	Sextet 2-tet	44.32	0.20	− 0.06	0.55	15.0
	Sextet 3-oct	41.14	0.29	0.006	0.29	28.0
	Sextet 4-oct	36.31	0.32	− 0.003	0.97	41.3
950	Sextet 1-oct	47.3	040	0.04	0.24	1.6
	Sextet 2-tet	45.1	0.29	0.03	0.38	14.7
	Sextet 3-oct	42.5	0.30	− 0.02	0.56	35.3
	Sextet 4-oct	38.2	0.31	− 0.01	0.81	48.3
1050	Sextet 1-oct	47.6	0.30	0.02	0.42	28.2
	Sextet 2-tet	46.0	0.25	0.03	0.23	13.4
	Sextet 3-oct	44.3	0.25	0.00	0.57	40.9
	Sextet 4-oct	40.2	0.30	− 0.06	0.63	17.5

4.2 Mössbauer spectroscopic analysis

The local information about structural and magnetic properties can be provided by the Mössbauer spectroscopy technique [49–51]. In the Mössbauer spectra, chemical environments and Fe ions exist at various sites with various coordination leads to various components in a sample. In a given sublattice, magnetically ordered ferric ions lead to a sextet (Zeeman splitting pattern) magnetic component. A paramagnetic component given by a magnetically disordered Fe^{3+} sublattice is a singlet or a doublet. The doublet possesses quadrupole splitting. Quadrupole splitting depends upon the iron valence state, the iron site distortion, and the cubic symmetry deviation. When the electric field gradient interacts with the nuclear quadrupole moment of Fe nucleus, it leads to a type of splitting called quadrupole splitting. To know the occupation of Fe ions at two crystallographic sites in spinel ferrite, the local structure, and hyperfine interactions, all heated samples were characterized by Mössbauer spectrosscopy technique at room temperature.

Mössbauer spectra of MgFe$_2$O$_4$ ferrite samples heated at 650 °C, 750 °C, 850 °C, 950 °C, and 1050 °C are presented in Fig. 7. In spinel ferrite, cations occupy the tetrahedral A-site and octahedral B-site in two magnetic sublattices. The magnitude of isomer shift (δ) is base for the cation's distribution. In this separation, (δ) at B-site is more than that of A-site [52–55]. The Mössbauer spectra of MgFe$_2$O$_4$ ferrite are fitted with four sextets. Thus, the tetrahedral site has one subspectrum (sextet 2) and octahedral sites have three subspectra (sextet 1, 3 and 4). The Mössbauer spectrum of bulk spinel possess two components; one from the tetrahedtal (A) site and other from the octahedral (B) site. In the present case, the four sextets are observed due to different particle sizes presented at tetrahedtal (A) site and octahedral (B) site.

Table 4 represents the results of Mössbauer spectral analysis at room temperature of MgFe$_2$O$_4$ samples heated at 650 °C, 750 °C, 850 °C, 950 °C, and
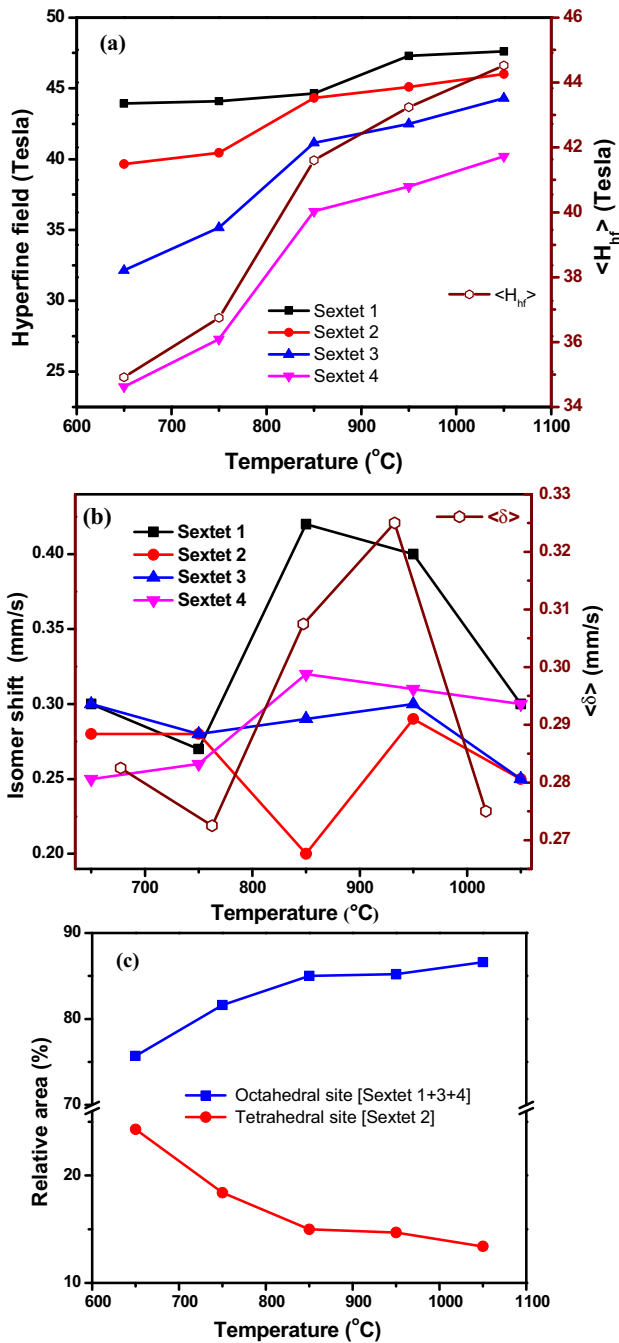
Fig. 8 a Variation in hyperfine field (H_{hf}), average hyperfine field ($< H_{\mathrm{hf}} >$), **b** isomer shift (δ), average isomer shift ($< \delta >$) ,and **c** relative area of tetrahedral site (sextet 2) and octahedral site (sextet 1 + 3 + 4)

1050 °C. The variation in the hyperfine magnetic field (H_{hf}), isomer shift, the relative area of tetrahedral site (sextet 2), and octahedral site (sextet 1 + 3 + 4) are presented in Fig. 8(a–c respectively). The hyperfine fields of all sextets are found to increase with increasing the heating temperature (Fig. 8a). The

assignment of sextets for two individual sites is accomplished on the basis of the values of isomer shift, hyperfine magnetic field, and relative area of sextets. In $MgFe_2O_4$, the tetrahedral site has lower value of the hyperfine field compared to the octahedral site for samples heated at 1350 and 1450 °C [56]. In the present work, sextet 2 is having less δ value between 0.2 and 0.29 mms^{-1} considered to be tetrahedral site [57, 58] and remaining all three sextets (1, 3, and 4) belong to the octahedral site. Isomer shift for B-site is found to be in the range of 0.25–0.42 mm s^{-1} [59, 60]. The values of δ for both sites are in the range of 0.2–0.42 mm s^{-1}, which confirmed that the Fe cations are in only Fe^{3+} high spin state, and Fe^{2+} is absent [61–63]. The variation has been observed in isomer shift with heating the sample, which means that the s-electron charge distribution of ferric ion is influenced by the heating also disturbance in the charge distribution of the ions surrounding Fe^{3+} ions [64]. The relative area of the tetrahedral site is found to be decreased with an increase the heating temperature (Fig. 8c). Mössbauer spectroscopic analysis supports the magnetization data, as (M_S) value raises with heating because of dsite preference of Mg ions at the tetrahedral site with increasing the heating temperature. Table 5 shows the cations distribution of $MgFe_2O_4$ synthesized in the presence of *solanum lycopersicum* fruit extract and heated at different temperatures for 4 h.

4.3 Dielectric properties

The dielectric property of ferrite depends on various factors like density, cation distribution, chemical composition, and synthesis method used to prepare samples and crystallite size, etc.[65, 66].

The dielectric constant (real-ε′) was calculated using the following relation:

$$\varepsilon' = \frac{C_p t}{\varepsilon_0 A} \tag{1}$$

where C_p = capacitance of the pellet (in faraday) t = thickness of the pellet in meter. ε_0 = permittivity in free space, *and* A = cross-sectional area of electrode.

The variation in dielectric constant (real-ε′) of $MgFe_2O_4$ spinel ferrite samples as a function of frequency is shown in Fig. 9a. It is clear from Fig. 9a that dielectric constant decreases fast in low-frequency regime; then it displays the nearly same value

Table 5 The cations distribution of $MgFe_2O_4$ ferrite samples synthesized in the presence of *solanum lycopersicum* extract and heated at different temperatures for 4 h

Heating temperature (°C)	Cation distribution (Mössbauer analysis)	Cation distribution (XRD: Rietveld refinement)
650	$(Mg_{0.51}Fe_{0.49})_{Tet} [(Mg_{0.49}Fe_{1.51}]_{Oct}O_4$	$(Mg_{0.50}Fe_{0.50})_{Tet} [(Mg_{0.50}Fe_{1.50}]_{Oct}O_4$
750	$(Mg_{0.63}Fe_{0.37})_{Tet} [(Mg_{0.37}Fe_{1.63}]_{Oct}O_4$	$(Mg_{0.64}Fe_{0.36})_{Tet} [(Mg_{0.36}Fe_{1.64}]_{Oct}O_4$
850	$(Mg_{0.7}Fe_{0.3})_{Tet} [(Mg_{0.3}Fe_{1.7}]_{Oct} O_4$	$(Mg_{0.7}Fe_{0.3})_{Tet} [(Mg_{0.3}Fe_{1.7}]_{Oct} O_4$
950	$(Mg_{0.704}Fe_{0.296})_{Tet} [(Mg_{0.296}Fe_{1.704}]_{Oct}O_4$	$(Mg_{0.72}Fe_{0.28})_{Tet} [(Mg_{0.72}Fe_{1.28}]_{Oct}O_4$
1050	$(Mg_{0.73}Fe_{0.27})_{Tet} [(Mg_{0.27}Fe_{1.73}]_{Oct}O_4$	$(Mg_{0.74}Fe_{0.26})_{Tet} [(Mg_{0.26}Fe_{1.74}]_{Oct}O_4$

(< 300 kHz) and it attributes to frequency-independent behavior after 300 kHz. This behavior is explained on the basis of Maxwell–Wagner's two-layer theory, which is in agreement with Koop's theory [67, 68]. According to this theory, the dielectric structure of ferrite is formed by two layers: the starting layer contains ferrite grains with good conductivity that is separated by weakly conducting grain boundary. After hopping of electrons, the electrons reach at the grain boundaries and pile up so that polarization occurs [69]. However, the movement of electrons is not able to follow up with increasing frequency, the possibility of electrons to arrive at grain boundaries is reduced and thus polarization reduces. Therefore, the dielectric constant observes fall with the increase in frequency [70, 71].

In the low-frequency regime, the dielectric constant decreases non-linearly with the increase in samples heating temperature from 650 °C to 1050 °C. The increase in samples heating temperature causes thermal activation of charge carriers, and thus, it increases the electronic hopping between Fe^{3+} and Fe^{2+} cations reducing the dielectric constant. It can be seen from SEM images (Fig. 5) that the increase in temperature renders to increase the grain size, but decreases the grain boundaries, which contribute to resistance. As a result, the applied field can pass through the grains easily, thus dielectric constant decreases with the rise in temperature from 650 °C to 1050 °C. The other reason for fall in ε' with temperature is associated with lattice vibrations and lattice energy dissipation due to internal friction of dipoles.

The dielectric loss tangent (tan δ) value for all samples was calculated using the Eq. (2):

$$\tan \delta = \frac{\varepsilon''}{\varepsilon'} \tag{2}$$

here ε' = real part of dielectric constant and ε'' = dielectric loss.

The variation in dielectric loss tangent with frequency is shown in Fig. 9b. It is noticed that as the frequency of applied ac field increases, the tan δ fall attributes to the usual nature of several ferrite materials. The energy dissipation measures the dielectric loss of the system. Various factors like Fe_2O_3 content, stoichiometric amount, the heating temperature of samples, and homogeneity of structure affect the value of tan δ [66, 72]. The loss factor decreases as frequency increases due to decreasing in hopping of electron as mentioned in Koop's phenomenological theory.

4.3.1 Frequency-dependant dielectric modulus

In ferrites, the complex electric modulus was used to study and analyze the electrical transport mechanism [73]. Figure 10a depicts the variation in the real dielectric modulus (M') with frequency and it confines near to zero value in the low-frequency region. The appreciable increase in M' is seen after 100 kHz and slope of M' increases with increase in temperature. At different temperatures, M' tends to saturate at 2 MHz, which suggests the short-range mobility of carriers in a conduction process [74, 75]. These observations are presumably due to the absence of restoring force which governs the mobility of charge carriers with the influence of an induced electric field. It also clarifies that the electrode polarization owes a negligible contribution to the ferrite [76].

The real (M') and imaginary (M'') components of dielectric modulus were calculated using relations (3) and (4):
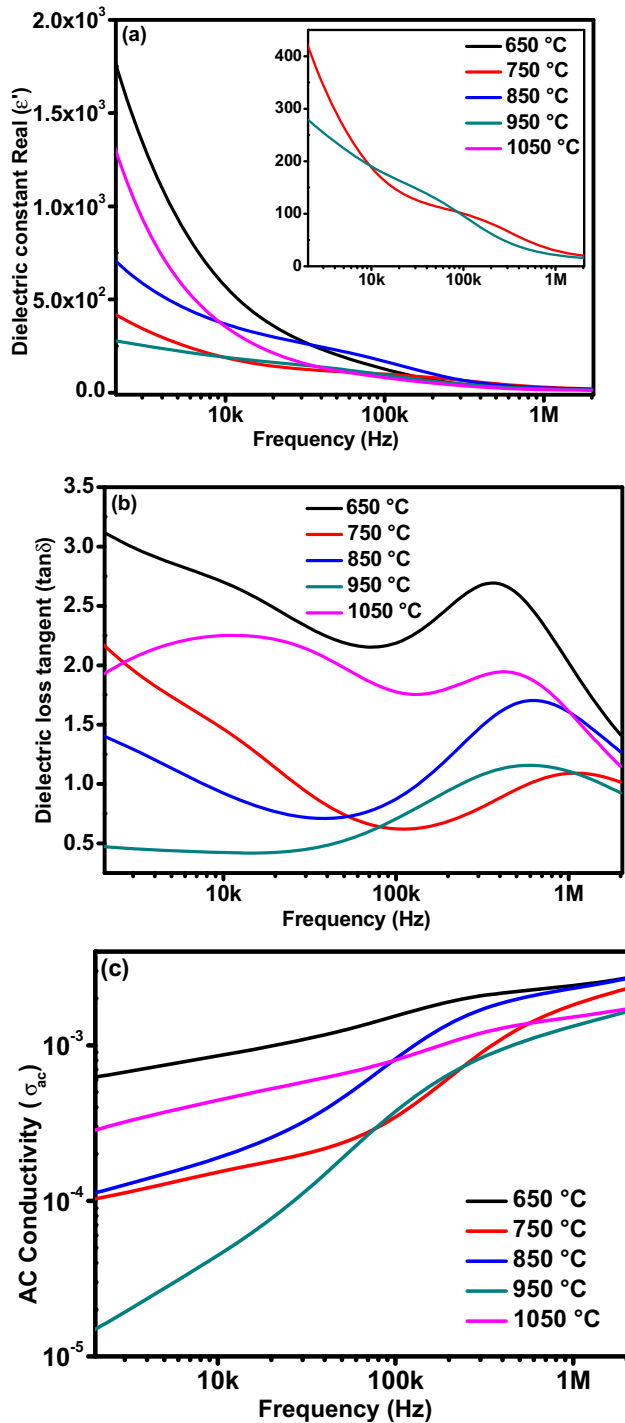
Fig. 9 Variation in **a** dielectric constant real (ε'), **b** loss tangent (tan δ), and **c** AC conductivity as a function of frequency for MgFe$_2$O$_4$ synthesized in the presence of *solanum lycopersicum* extract

$$M' = \frac{\varepsilon'}{\varepsilon'^2 + \varepsilon''^2} \tag{3}$$

$$M'' = \frac{\varepsilon''}{\varepsilon'^2 + \varepsilon''^2} \tag{4}$$

where ε' is real part of dielectric constant and ε'' is dielectric loss.

Figure 10b depicts the variation in imaginary dielectric modulus (M'') as a function of frequency. It shows that as frequency increases, the imaginary part of modulus also increases.

Figure 10c shows clearly resolved half semi-circles for all the samples synthesized in the presence of *Solanum Lycopersicum* extract. A single half semi-circle arc can be clearly seen for the samples heated at 650 °C and 1050 °C.

The sample heated at 650 °C shows straight line from 20 Hz to 100 kHz and thereafter one semi-circular arc is observed till the end of the test frequency range (1.78 MHz). This arc is consistent with the second relaxation observed in the loss tangent parameter (Fig. 9b) in the high-frequency regime. However, no arc of M'-M'' in the low-frequency regime implies presence of first peak of loss tangent as conductivity relaxation. However, in the sample heated at 750 °C, it shows two semi-circle arcs in the low- and high-frequency regions ascribing dielectric relaxation in the peaks of tan δ. Similarly, two relaxation peaks were observed for tan δ at 850 °C. Three regions are seen for the sample heated at 950 °C: region 1-first semi-circular arc is visible from 20 Hz to 3 kHz, region 2- a straight line from 3 to 15 kHz, region 3- a semi-circular arc is observed for rest of the frequency region. This variation is in accordance with tan δ wherein depressed peak of relaxation towards low-frequency regime is as per region 1, nearly constant loss tangent for region 2 and second relaxation for region 3. For the sample heated at 1050 °C; there is a slight depression between two visible semi-circular arcs and it is in agreement with two adjacent relaxations in tan δ. The increase in temperature renders non-linear movement of semi-circular arcs towards high-frequency region, which further consolidates the grains effect and reduces the grain boundaries effect.

4.3.2 Frequency-dependant dielectric Impedance

Figure 11a, b illustrate the relationship between the real and imaginary part of impedance with frequency. The impedance analysis is the best tool to
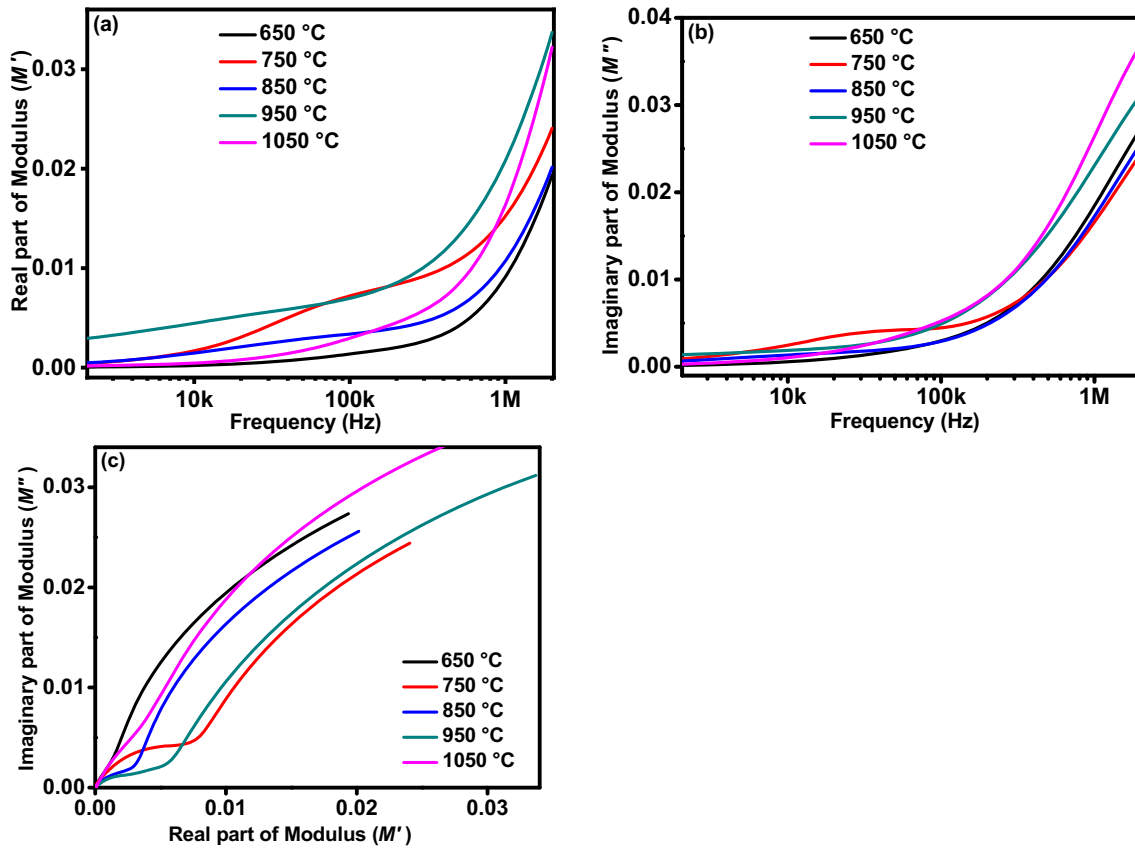
Fig. 10 Variation in **a** real part of dielectric modulus (M') and **b** imaginary part of dielectric modulus (M'') as a function of frequency and **c** real part of dielectric modulus (M') verses Imaginary part of dielectric modulus (M'') for MgFe$_2$O$_4$ spinel ferrites synthesized in the presence of *solanum lycopersicum* fruit extract
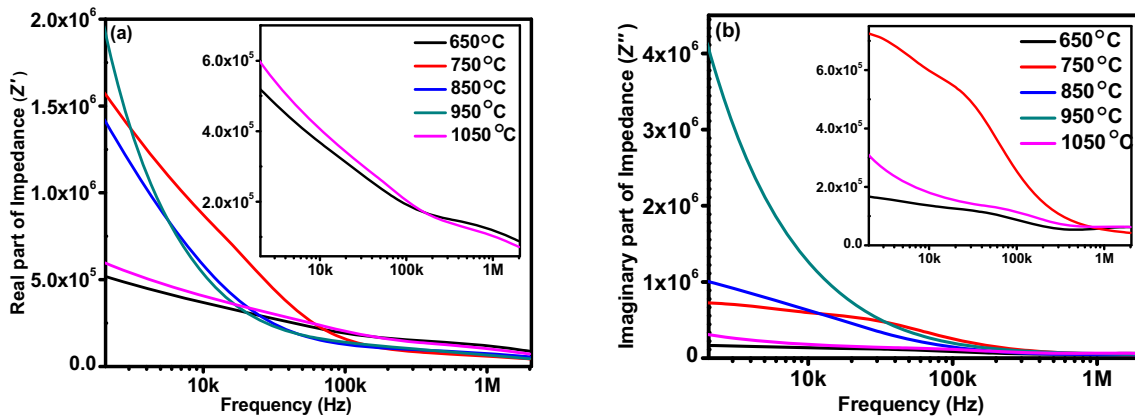

Fig. 11 Variation in **a** dielectric Impedance real (Z'-(ohm)) and **b** dielectric impedance Imaginary (Z''(ohm))) as a function of frequency for MgFe$_2$O$_4$ spinel ferrites synthesized in presence of *solanum lycopersicum* extract

know about the electrical properties of synthesized spinel ferrites. This method gives information for the real (resistive) part and the imaginary (reactive) part which contributes to conduction on the application of an *ac* electric field [77, 78].

Generally, the real (Z') as well as imaginary (Z'') components of the impedance are based on resistance (R_p) and capacitance (C_p) of grain and grain boundary as shown in relations (5) and (6) as follows:
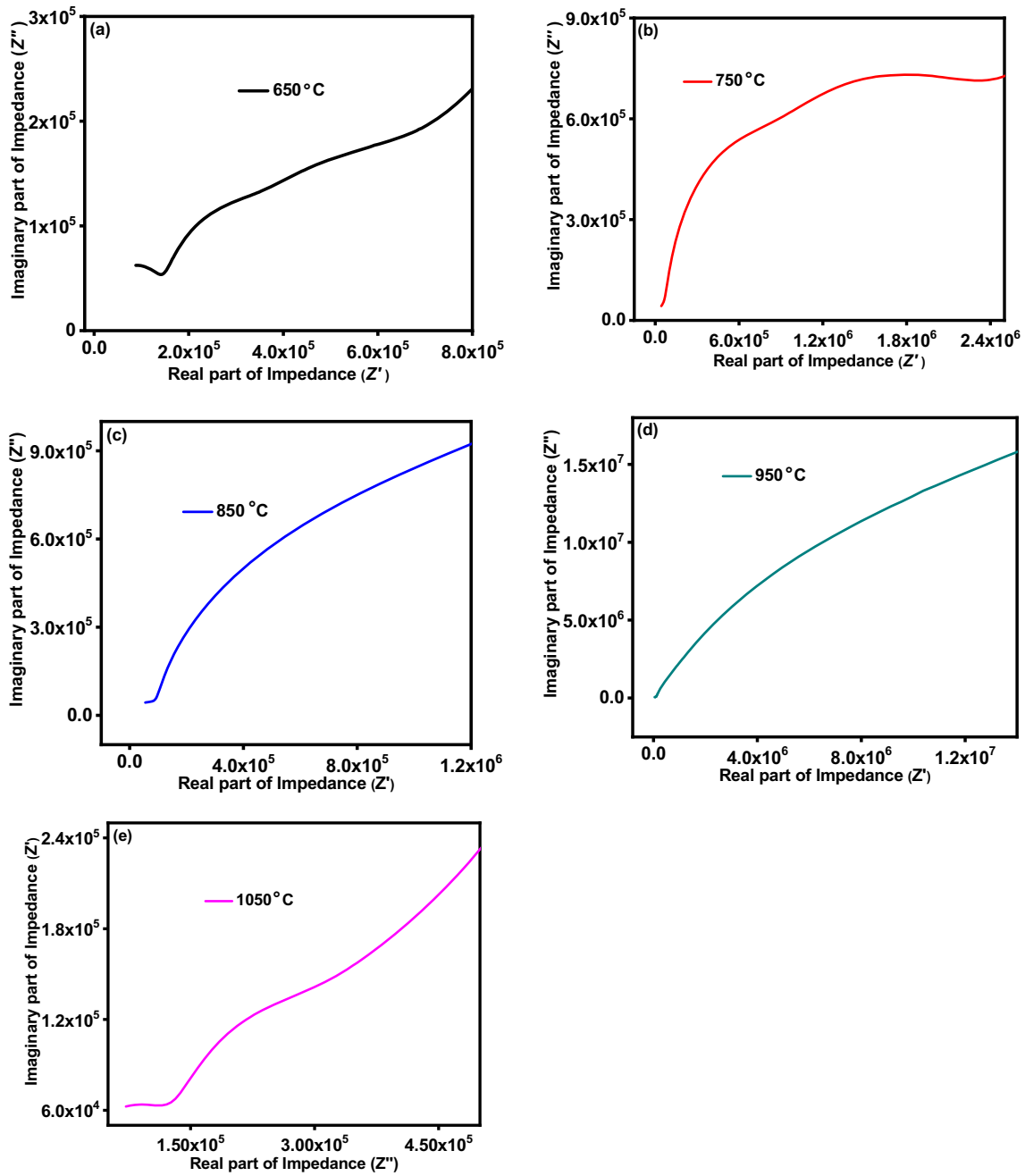
Fig. 12 **a–e** Real part of dielectric impedance (Z′(ohm))) versus Imaginary part of dielectric impedance (Z″(ohm))) heated at various temperature

$$Z' = \frac{R_p}{1 + \left(\omega C_p R_p\right)^2} \ (ohm) \tag{5}$$

$$Z'' = \frac{\omega C_p R_p^2}{1 + \left(\omega C_p R_p\right)^2} \ (ohm) \tag{6}$$

For all samples heated at various temperatures, there is an observation of the decrease in Z′ with an increase in frequency. It can be associated with the decrease in space charge polarization in the high-frequency region [78]. The decreasing trend of Z′ with increasing frequency shows that conductivity of the material increases with an increase in frequency. A large dispersion is observed in the low-frequency regime with the increase in heating temperature of samples from 650 °C to 750 °C, 850 °C, and 950 °C.
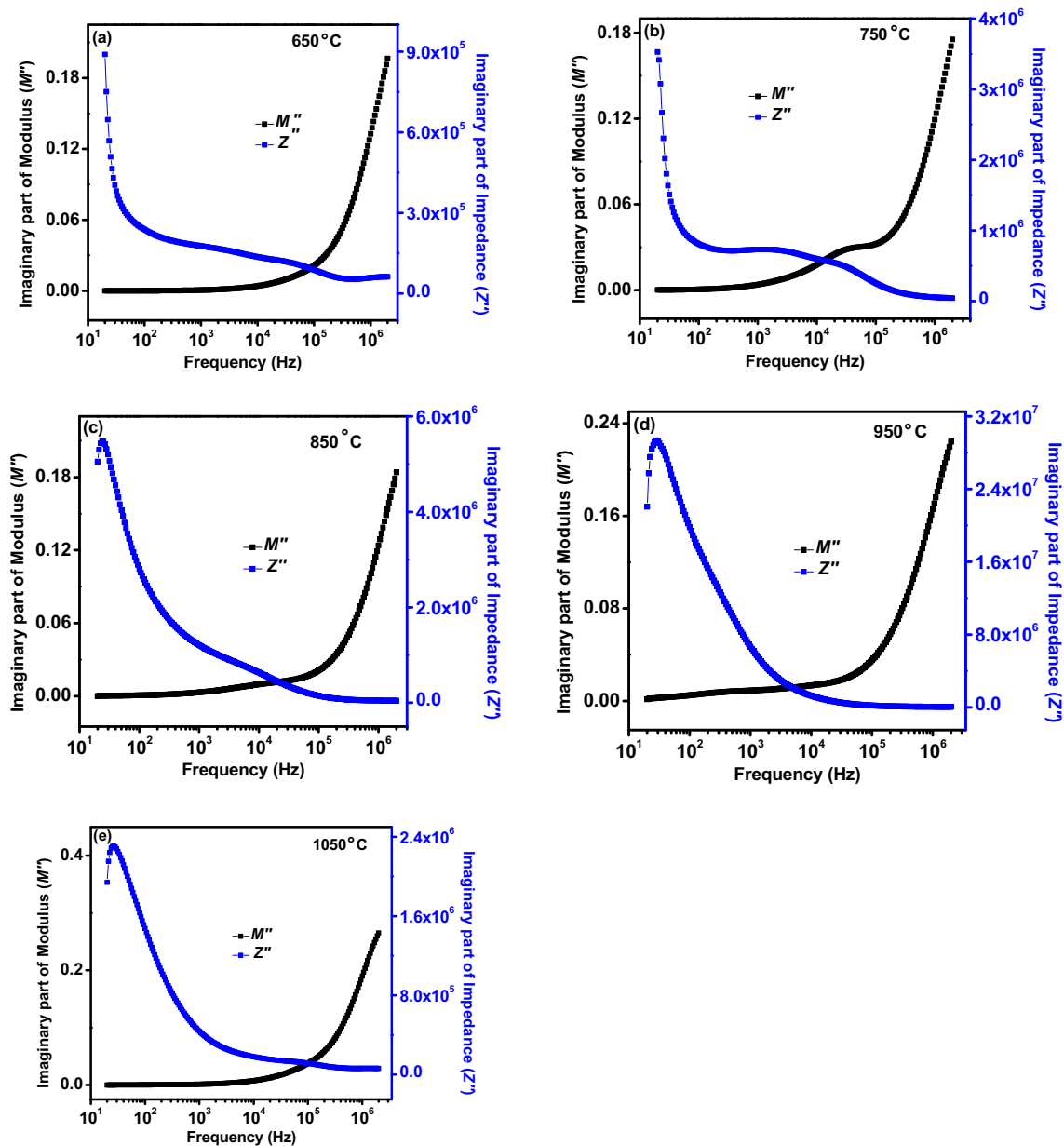
Fig. 13 a–e Imaginary part of modulus (M''), imaginary part of impedance (Z'') versus frequency (Hz)

However, further rise in temperature to 1050 °C causes abrupt fall in Z' close to the value observed at 650 °C. The imaginary part of impedance (Z'') is also found to decrease as the frequency increases. It increases with the temperature from 650 °C, 750 °C, 850 °C, and 950 °C and decreases abruptly at 1050 °C. The plots of Z'' merge with each other in the frequency regime and are not able to distinguish from each other.

The distribution in Nyquist plot can be understood by considering the two layers model and these plots show two semi-circular curves. The semi-circular curves at low-frequency and at high-frequency regions are because of the contribution of grain boundary and the grain, respectively. The nature of curves in Nyquist plot depends upon grains size. The materials having lower grains size indicate only one semi-circle, while higher grains size lead to double semi-circles [79]. It is clear from Fig. 12a–e that there are only single one-fourth semi-circles at lower-frequency region indicating that the conduction occurs due to the grain boundaries over the grain conductions [80].

Figure 13a–e display a graph of M'' and Z'' with the dependence of frequency for different temperature. In order to confirm Debye relaxation peaks, M'' and Z'' should overlap at a specific frequency [69]. The graphs depict the non-existence of this criterion indicating the absence of Debye relaxation in prepared magnesium ferrites at all temperatures.

5 Conclusions

Spinel $MgFe_2O_4$ ferrite powder was synthesized in the presence of tomato fruit extract using the sol–gel auto-combustion technique at various temperatures. XRD analysis confirms the formation of single spinel phase and lattice constant value is found to increase with increasing the heating temperature. Formed magnesium ferrites belong to magnetically soft ferrites (H_C = 10 Oe–70 Oe) and possess a multi-domain structure. The values of M_S, M_r, H_C, and H_{hf} are found to increase with increasing the heating temperature of the sample. The value of saturation magnetization lies in the range of 14.28 emu/g to 30.80 emu/g. An average grain size varies from 18 nm to 65 nm. The sample heated at 1050 °C shows larger grains compared to other samples. Dielectric measurements demonstrate the frequency-dependent phenomena for all samples. All samples show single one-fourth semi-circles in Nyquist plot because of the contribution of the grain boundaries over grain conductions.

References

1. R. Srivastava, B. Yadav, Int. J. Green Nanotechnol. **4**, 141 (2012)
2. A. Verma, T. Goel, R. Mendiratta, R. Gupta, J. Magn. Magn. Mater. **192**, 271 (1999)
3. T. Nakamura, T. Miyamoto, Y. Yamada, J. Magn. Magn. Mater. **256**, 340 (2003)
4. J. Smit, H. Wijn, Ferrites (New York 1959).
5. M. Sugimoto, J. Am. Ceram. Soc. **82**, 280 (1999)
6. C. Srinivas, E.R. Kumar, B.V. Tirupanyam, S.S. Meena, P. Bhatt, C.L. Prajapat, C. Rao, D.L. Sastry, J. Magn. Magn. Mater. **502**, 166534 (2020)
7. M. Srivastav, S.K. Alla, S.S. Meena, N. Gupta, R.K. Mandal, N.K. Prasad, Ceram. Int. **45**, 12028 (2019)
8. M. Srivastava, S.S. Meena, R.K. Mandal, S.M. Yusuf, N.K. Prasad, J. Alloys Compd. **688**, 219 (2016)
9. M.G. Naseri, E.B. Saion, Adv. Cryst. Proc. **43**, 352 (2012)
10. D. Chen, D. Zeng, Z. Liu, Mater. Res. Express. **3**, 045002 (2016)
11. S. Katlakunta, S.S. Meena, S. Srinath, M. Bououdina, R. Sandhya, K. Praveena, Mater. Res. Bull. **63**, 58 (2015)
12. D. Chen, Y. Meng, D. Zeng, Z. Liu, H. Yu, X. Zhong, Mater. Lett. **76**, 84 (2012)
13. D. Chen, Y. Meng, K. Gandha, D. Zeng, H. Yu, P. Liu, AIP Adv. **7**, 056214 (2017)
14. M. Hashim, S. Shirsath, S.S. Meena, M. Mane, S. Kumar, P. Bhatt, R. Kumar, N. Prasad, S. Alla, J. Shah, R. Kotnala, K. Mohammed, E. Senturk, J. Alloy Compd. **642**, 70 (2015)
15. P. Kaur, S.K. Chawla, S.S. Meena, S.M. Yusuf, K. Pubby, S. Bindra Narang, Ceram. Int. **43**, 590 (2017)
16. S.K. Chawla, R.K. Mudsainiyan, S.S. Meena, S.M. Yusuf, J. Magn. Magn Mater. **350**, 23 (2014)
17. Y. Wang, Y. Huang, Q. Wang, J. Magn. Magn Mater. **324**, 3024 (2012)
18. R. Waldron, Phys Rev. **99**, 1727 (1955)
19. R.V. Upadhyay, R.G. Kulkarni, Mater. Res. Bull. **19**, 655 (1984)
20. K.B. Modi, H.H. Joshi, R.G. Kulkarni, J. Mater. Sci. **31**, 1311 (1996)
21. F. Gandomi, S.M. Motlagh, M. Rostami, A.S. Nasab, M.F. Ramandi, M.E. Arani, R. Ahmadian, N. Gholipour, M.R. Nasrabadi, M.R. Ganjali, J Mater Sci: Mater Electron. **30**, 19691 (2019)
22. S.M. Motlagh, A.S. Nasab, R. Mojtaba, S. Hossein, M.E. Arani, M.F. Ramandi, M.R. Ganjali, M.R. Nasrabadi, J Mater Sci: Mater Electron. **30**, 6902 (2019)
23. M.R. Nasrabadi, M. Behpour, S.N. Ali, M.R. Jeddy, J Mater Sci: Mater Electron. **27**, 11691 (2016)

24. A. Manikandan, M. Durka, S. Antony, J. Inorg. Organomet. Polym. **25**, 1019 (2015)

25. D. Gingasu, I. Mindru, S. Preda, J. Calderon-Moreno, D. Culita, L. Patron, L. Diamandescu, Rev. Roum. Chim. **62**, 645 (2017)

26. A. Ben-Arfa, I.M. Basam, J. Salvado, R.C.P. Ferreira, J. Alloys Compd. **786**, 71 (2019)

27. S. Fardood, A. Ramazani, S. Moradi, J. Sol-Gel Sci. Technol. **82**, 432 (2017)

28. K. Kombaiah, J. Vijaya, L. Kennedy, M. Bououdina, R. Ramalingam, H. Al-Lohedan, Mater. Chem. Phys. **204**, 410 (2018)

29. G.R. Beecher, Nutrient content of tomato and tomato products, (Food Composition Laboratory, Beltsville Human Nutrition Research Center, ARS, USDA, 1998)

30. Safety Assessment of transgenic organism in the environment, OECD Consensus Documents, Volume 7 (2017) 70

31. S. Clinton, C. Emenhiser, S. Schwartz, D. Bostwick, A. Williams, B. Moore, J. Erdman, Cancer Epidemiol. Biomark. **5**, 823 (1996)

32. A. Pradeep, P. Priyadharsini, G. Chandrasekaran, J. Magn. Magn. Mater. **320**, 2774 (2008)

33. U. Ozgur, Y. Alivov, H. Morkoc, J. Mater. Sci.: Mater. Electron. **20**, 789 (2009)

34. W.V. Aulock, *Handbook of Microwaves Ferrites* (Materials Academic Press, New York, 1965)

35. V. Naidu, S. Ahamed, K. Sahib, M. Suganthi, C. Prakash, Int. J. Comput. Appl. **27**, 40 (2011)

36. M.M. Hessien, Z.I. Zaki, Q. Mohsen, Int. J. Mech. Sci. **1**, 30 (2011)

37. S. Kanagesan, M. Hashim, S. Tamilselvan, N.B. Alitheen, I. Ismail, G. Bahmanrokh, J Nanomater. **8** (2013)

38. M. Pavlovic, C. Jovalekic, A. Nikolic, D. Manojlovic, N. Sojic, J. Mater. Sci.: Mater. Electron. **20**, 782 (2009)

39. R. Kotnala, J. Shah, B. Singh, H. Kishan, S. Singh, S. Dhawan, A. Sengupta, Sens. Actuators B **129**, 909 (2008)

40. M. Raju, Chem. Sci. Trans. **4**, 137 (2015)

41. A. Pradeep, Chandrasekaran, Mater Lett. **60**, 371 (20

42. S. Jain, K. Adiga, V. PaiVerneker, Combust. Flame. **40**, 71 (1981)

43. S. Ali Ridha, J. Compos. Mater. **5**, 195 (2015)

44. A. Loganathan, K. Kumar, Appl. Nanosci. **6**, 629 (2016)

45. K. Modi, M. Chhantbar, H. Joshi, Ceram. Inter. **32**, 111 (2006)

46. C. Dong, J. Appl. Crystallogr. **32**, 838 (1999)

47. C. Vestal, Z. Zhang, J. Am. Chem. Soc. **125**, 9828 (2003)

48. S. Assar, H. Abosheiasha, J. Magn. Magn Mater. **374**, 264 (2015)

49. D. Dickson, F. Berry (eds.), *Mössbauer Spectroscopy* (Cambridge University Press, Cambridge, 1986)

50. U. Gonser (ed.), *Mössbauer Spectroscopy* (Springer, New York, 1975)

51. H. Shalgosky, N. Greenwood, T. Gibb, *Mossbauer Spectroscopy* (Chapman and Hall Ltd, London, 1973)

52. S.S. Shinde, S.S. Meena, S.M. Yusuf, K.Y. Rajpure, J. Phys. Chem. **115**, 3731 (2011)

53. K. Sharma, S.S. Meena, C.L. Prajapat, S. Bhattacharya, M.R. Singh, S.M. Yusuf, G.P. Kothiyal, J. Magn. Magn Mater. **321**, 3821 (2009)

54. S.M. Patange, S.S. Desai, S.S. Meena, S.M. Yusuf, S.E. Shirsath, RSC Adv. **5**, 91482 (2015)

55. S.P. Yadav, S.S. Shinde, P. Bhatt, S.S. Meena, K.Y. Rajpure, J. Alloy Compd. **646**, 550 (2015)

56. S.K. Durrani, S. Naz, M. Mehmood, M. Nadeem, M. Siddique, J. Saudi Chem. Soc. **21**, 899 (2017)

57. K. Sharma, A. Dixit, S.S. Meena, Jagannath, S. Bhattacharya, C.L. Prajapat, P.K. Sharma, S.M. Yusuf, A.K. Tyagi, G.P. Kothiyal, Mater. Sci. Eng. C **29**, 2226 (2009)

58. K. Sharma, S.S. Meena, S. Saxena, S.M. Yusuf, A. Srinivasan, G.P. Kothiyal, Mater. Chem. Phys. **133**, 144 (2012)

59. K. Sharma, C.L. Prajapat, S.S. Meena, M.R. Singh, S.M. Yusuf, L. Montagne, G.P. Kothiyal, J. Magn. Magn. Mater. **345**, 24 (2013)

60. A. Gangwar, S.K. Alla, M. Srivastava, S.S. Meena, E.V. Prasadrao, R.K. Mandal, S.M. Yusuf, N.K. Prasad, J. Magn. Magn. Mater. **401**, 559 (2016)

61. P.P. Naik, R.B. Tangsali, S.S. Meena, S.M. Yusuf, Mater. Chem. Phys. **191**, 215 (2017)

62. B.V. Tirupanyam, C. Srinivas, S.S. Meena, S.M. Yusuf, A.S. Kumar, D.L. Sastry, V. Seshubai, J. Magn. Magn. Mater. **392**, 101 (2015)

63. K.S. Ramakrishna, C. Srinivas, S.S. Meena, B.V. Tirupanyam, P. Bhatt, S.M. Yusuf, C.L. Prajapat, D.M. Potukuchi, D.L. Sastry, Ceram. Int. **43**(11), 7984 (2017)

64. K. Pubby, S.S. Meena, S.M. Yusuf, S.B. Narang, J. Magn. Magn. Mater. **466**, 430 (2018)

65. G. Rana, U. Johri, K. Asokan, Europhys. Lett. **103**, 17008 (2013)

66. A.R. Kagdi, N.P. Solanki, F.E. Carvalho, S.S. Meena, P. Bhatt, R.C. Pullar, R.B. Jotania, J. Alloy Compd. **741**, 377 (2018)

67. A. Wagner, J. Phys. **48**, 817 (1973)

68. J. Maxwell, *Electricity and Magnetism* (Oxford University, London, 1973)

69. J.R. Macdonald, *Impedance Spectroscopy: Emphasizing Solid State Material and Systems* (Wiley, New York, 1987)

70. P. Shaikh, R. Kamble, A. Rao, Y. Kolekar, J. Alloy Compd. **482**, 276 (2009)

71. A. Bhavikatti, S. Kulkarni, A. Lagashetty, Int. J. Eng. Sci. Technol. **3**, 5985 (2011)

72. S. Dutta, R. Choudhry, P. Sinha, Phys. Status Solidi. **202**, 1172 (2005)

73. P. Macedo, Phys. Chem. Glasses **13**, 171 (1972)

74. S. Saha, T.P. Sinha, Phys. Rev. B **65**, 1341 (2005)

75. K.P. Padmasree, D.D. Kanchan, A.R. Kulkami, Solid State Ion. **177**, 475 (2006)

76. B.V. Chowdari, R. Gopalkrishnnan, Solid State Ion. **23**, 225 (1987)

77. S. Sindhu, M. Anantharaman, B. Thampi, K. Malini, P. Kurian, Bull. Mater. Sci. **25**, 599 (2002)

78. A. Pradhan, T. Nath, S. Saha, Mater. Res. Express **4**, 076107 (2017)

79. K. Batoo, Physica B **406**, 382 (2011)

80. M. Hashim, S. Kumar, B.H. Koo, S.E. Shirsath, E.M. Mohammed, J. Shah, R.K. Kotnala, H.K. Choi, H. Chung, R. Kumar, J. Alloys Compd. **518**, 11 (2012)